Solid oxide cell electrode nanocomposites fabricated by inkjet printing infiltration of ceria scaffolds

(Article begins on next page)

23 November 2024

Solid Oxide Cell Electrode Nanocomposites Fabricated by Inkjet Printing Infiltration of Ceria Scaffolds

Simone Anelli [1] , **Luis Moreno-Sanabria** [2] , **Federico Baiutti** [1] , **Marc Torrell** [1] **and Albert Tarancón** [1,3,*]

[1] Department of Advanced Materials for Energy, Catalonia Institute for Energy Research (IREC), Jardins de les Dones de Negre, 1, Sant Adrià de Besòs, 08930 Barcelona, Spain; sanelli@irec.cat (S.A.); fbaiutti@irec.cat (F.B.); mtorrell@irec.cat (M.T.)
[2] Institute of Ceramics and Glass (ICV-CSIC), Kelsen 5, 28049 Madrid, Spain; l.moreno@icv.csic.es
[3] ICREA, Passeig Lluís Companys 23, 08010 Barcelona, Spain
[*] Correspondence: atarancon@irec.cat

Abstract: The enhancement of solid oxide cell (SOC) oxygen electrode performance through the generation of nanocomposite electrodes via infiltration using wet-chemistry processes has been widely studied in recent years. An efficient oxygen electrode consists of a porous backbone and an active catalyst, which should provide ionic conductivity, high catalytic activity and electronic conductivity. Inkjet printing is a versatile additive manufacturing technique, which can be used for reliable and homogeneous functionalization of SOC electrodes via infiltration for either small- or large-area devices. In this study, we implemented the utilization of an inkjet printer for the automatic functionalization of different gadolinium-doped ceria scaffolds, via infiltration with ethanol:water-based $La_{1-x}Sr_xCo_{1-y}Fe_yO_{3-\delta}$ (LSCF) ink. Scaffolds based on commercial and mesoporous Gd-doped ceria (CGO) powders were used to demonstrate the versatility of inkjet printing as an infiltration technique. Using yttrium-stabilized zirconia (YSZ) commercial electrolytes, symmetrical LSCF/LSCF–CGO/YSZ/LSCF–CGO/LSCF cells were fabricated via infiltration and characterized by SEM-EDX, XRD and EIS. Microstructural analysis demonstrated the feasibility and reproducibility of the process. Electrochemical characterization lead to an *ASR* value of $\approx 1.2~\Omega~cm^2$ at 750 °C, in the case of nanosized rare earth-doped ceria scaffolds, with the electrode contributing $\approx 0.18~\Omega~cm^2$. These results demonstrate the feasibility of inkjet printing as an infiltration technique for SOC fabrication.

Keywords: inkjet printing; solid oxide fuel cells; infiltration; mesoporous; oxygen electrode; electrochemistry

1. Introduction

Solid oxide cells (SOCs) are devices which can reversibly produce and utilize hydrogen for chemical to electrical energy conversion with high efficiency [1–6]. State-of-the-art (SoA) materials for SOCs are ionic conductors such as yttrium-stabilized zirconia (YSZ) and Gd-doped ceria (CGO) for the electrolyte, Ni-YSZ ceramic metallic composites for the fuel electrode and mixed ionic–electronic conductors (MIECs) such as $La_{1-x}Sr_xCo_{1-y}Fe_yO_{3-\delta}$ (LSCF) for the oxygen electrode [7]. Composite electrodes involving MIEC perovskites together with pure ionic conductors (e.g., YSZ and CGO) improve the performance of the cell, increasing the active region of the electrode called the triple phase boundary (TPB). The TPB is the region where ions, electrons and the gas are in contact and where oxygen reduction reactions (ORRs) take place during operation in the fuel cell mode [8–10]. Although employing an electrolyte material in electrode composites increases chemical and thermo-mechanical compatibility, the required high-temperature treatments present some drawbacks. One of the most important is the formation of insulating secondary phases between SoA strontium-rich perovskites and zirconia-based electrolytes (i.e., $La_2Zr_2O_7$ and $SrZrO_3$) [11–13]. To improve compatibility, barrier layers of ceria are commonly introduced between the electrolyte and the oxygen electrode [14,15]. Barrier layers demonstrate the

ability to grant great stability at the electrolyte–electrode interface during high-temperature fabrication and operation [14]. Moreover, low-temperature synthesis of infiltrated perovskites inside a pre-sintered electrolyte scaffold, which substantially further reduces the formation of unwanted phases, has also been recently demonstrated to be particularly effective [16–18]. Infiltration typically requires low amounts of active material (metal–salt solutions [19], nanoparticles in suspension [17] or molten salts [20]), resulting in well-distributed nanosized and nanostructured electrodes [18]. To ensure proper dispersion of the solution, the use of different additives such as urea, citric acid, glycine, and ethylene glycol [19] is required. The use of pre-sintered scaffolds with ordered structure and small porosity can promote the fabrication of functional layers with high active areas and proper distribution of the infiltration solution. In particular, nanocomposites based on mesoporous ceria backbones demonstrate excellent performance as electrodes for SOC applications [21–24]. Mesoporous materials are characterized by small porosity (2–50 nm in diameter), a high surface area (>100 m^2 g^{-1}) [25–27], and good percolation pathways, which mitigate problems associated with local high current densities in SOC operation [28–37]. The synthesis of mesoporous materials typically involves the impregnation of sacrificial templates such as SiO_2 that, after calcination, are removed by chemical etching. In particular, nanocasting using hard templates allows the fabrication of powders with high ordered structures and complex lattices such as KIT-6 or SBA-15 [32,38–41].

Despite the above-mentioned advantages, infiltration is currently carried out manually with a micro-pipette [19,37,42–49] or via dip coating [50,51], compromising its reproducibility, robustness and scalability. The implementation of additive manufacturing (AM) techniques for the automation of infiltration steps, in particular using inkjet printing (IJP), is a possible solution to standardize the process [52–58]. IJP is a high-resolution printing technique where small droplets of ink (with a volume in the range of 1 nL^{-1} pL) are deposited on a substrate. In standard domestic IJP applications, black or cyan, yellow, magenta, black (CYMK) inks are deposited on paper but the technology has been broadly extended and it is now a very versatile technique. IJP is used for the deposition of submicronic particles (e.g., precious metal and ceramic materials) [59–61] in electronics [62], rapid prototyping [63], ceramic-based components [59,60] and sensors [64]. The viscosity range for ceramics-based inks for IJP is 1–20 mPa s and the deposited layer thickness is from below 100 nm up to 100 μm [65,66]. This, together with the low solid loading of the inks (1–10 vol%), makes IJP a time-consuming technique that is more suitable for low aspect ratios or 2D objects (opposite to other AM techniques that are more adequate for the fabrication of high-aspect ratio 3D parts) [67]. IJP is broadly classified as either continuous inkjet (CIJ) [59,68,69] or drop-on-demand (DOD) [59,70,71] printing. CIJ consists of a pressurized flow of ink which generates a continuous stream of drops through a micro-scaled nozzle. When printing is not required, the stream is deflected to a gutter for recycling [59]. On the other hand, DOD-IJP is based on a stream of droplets generated only when required for printing (avoiding unnecessary waste of material) [60,71]. Drop formation requires a pressurized liquid which generates droplets driven by Ryleigh instability.

DOD-IJP has been used in the field of SOCs to produce different components, from dense electrolytes [72] to composite electrodes by infiltration [56,57]. Typical inks used for DOD-IJP deposition of ceramic materials are colloidal suspension and sol–gel solutions. Such inks are usually characterized by densities of approximately ≈1 g cm^{-3}, viscosity in the range of 1–30 mPa s and surface tension in the range of 35–70 mN m^{-1} [73]. Optimal rheology of the inks is essential to avoid clogging of the nozzles, the formation of satellite drops [74] or splashing [61] of the liquid on the substrate. In the literature, the Reynolds (*Re*) and Weber (*We*) numbers are used to describe the properties of inks [59,75] either alone or combined together in the so-called Ohnesorge (*Oh*) number [59]. The most commonly employed rheological parameter is the inverse of the *Oh* number, called *Z*, and it is calculated following the next expression (Equation (1)) [71]:

$$Z = Oh^{-1} = \frac{Re}{\sqrt{We}} = \frac{\sqrt{\gamma \rho a}}{\eta} \tag{1}$$

where a is the average diameter of the droplet (which corresponds to the nozzle diameter) and ρ, η and γ are the density, the dynamic viscosity, and the surface tension of the ink, respectively. Z is a widely employed and reliable parameter because it is independent of the jetting speed and can be experimentally determined. Suitable printability ranges are usually accepted for $1 \leq Z \leq 10$ [76–78] and $1 \leq Z \leq 20$ [71], although the upper limit is not totally clear, since stable printing has even been reported at $Z >> 10$ [79,80], e.g., $Z = 100$ [81–83].

In this work, automatic infiltration of electrolyte scaffolds with active electrode materials is employed for the fabrication of functional layers in solid oxide cells. In particular, DOD-IJP is used to infiltrate mesoporous ceria-based pre-sintered backbones with LSCF. The performance of these composites is evaluated as oxygen electrodes in symmetrical cells consisting of YSZ/LSCF–CGO/LSCF. The produced cells were structurally, microstructurally and electrochemically characterized between 600 and 900 °C. Overall, the main goal of this study is to demonstrate the feasibility of IJP as an automatic infiltration technique for SOC application and to standardize the process for future application in large-area devices.

2. Materials and Methods

2.1. Formulation of LSCF Inks

To obtain a $La_{0.6}Sr_{0.4}Co_{0.2}Fe_{0.8}O_3$ perovskite, a solution 0.1 M of $La(NO_3)_3 \cdot 6H_2O$, $Sr(NO_3)_2$, $Co(NO_3)_2 \cdot 6H_2O$ and $Fe(NO_3)_3 \cdot 9H_2O$ (Merck, Darmstadt, Germany) was prepared in stoichiometric proportion. Polyvinylpyrrolidone (PVP—Merck, Darmstadt, Germany) the dispersant and glycine ($C_2H_5NO_2$—Merck, Darmstadt, Germany) as the complexing agent were dissolved in an ethanol:water (70:30 vol%) medium under continuous stirring at room temperature. After the complete dissolution of PVP and glycine, the precursors were added one by one, under continuous stirring. The formulation of the LSCF sol–gel solution was optimized for handmade infiltration in previous works of the group to achieve good permeability inside the ceramic backbone [35–37].

2.2. Rheological Characterization

A DV3T Rheometer (Brookfield Engineering Labs., Inc., 11 Commerce Boulevard, Middleboro, MA, USA) was used to measure the viscosity of the produced ink. The instrument can measure the viscosity of a liquid medium at given share rates. It has a speed rate which from 0.01 to 250 RPM, a viscosity accuracy of ±1.0% and a viscosity repeatability of approximately ±0.2%.

Surface tension measurement of the ink was made by an OCA20 optical contact angle and contour analysis system (DataPhysics Instruments GmbH, Filderstadt, Germany), using the pendant drop method. This method can determine the surface tension (σ) of a liquid medium from the Young–Laplace equation (Equation (2)).

$$\Delta p = \sigma \left(\frac{1}{r_1} + \frac{1}{r_2} \right) \tag{2}$$

In the equation, Δp is the difference in pressure between the two sides of the curved surface and r_1 and r_2 are the two curvature radii of the drop.

2.3. Symmetrical Cells Fabrication

Symmetrical electrolyte-supported cells were prepared using tape-casted 8YSZ (FAE S.A.U., L'Hospitalet de Llobregat, Barcelona, Spain) as electrolyte and cell support with a diameter of ≈2 cm and a thickness of ≈150 μm. A roughness promoter layer was sprayed on top of this this dense YSZ layer by 3-axis automated airbrushing (Print3D Solutions, Albacete, Spain) using ethanol-based ink with commercial $Ce_{0.8}Gd_{0.2}O_{1.9}$ powders (Kceracell, Geumsan, Korea) as the solid load. The coating was deposited on both sides of the YSZ

electrolyte and sintered at 1250 °C for 3 h. This layer was deposited in order to increase the roughness of the surface and to improve the attachment of the electrodes to the electrolyte, minimizing the contact resistance of the interfaces. A barrier layer of CGO, decorated with 5 wt% of Co oxide as sintering aid, was deposited on top of the roughness promoter layer to avoid reactivity between the YSZ and the LSCF layers. The barrier layer ($\approx$15 μm) was sintered at 1275 °C for 2 h (2 °C min^{-1}) before the deposition of the oxygen electrode [14]. Then, the different CGO scaffold layers (thickness $\approx$60 μm) were equally deposited on top using the same method. The composition of the inks for CGO airbrushing is detailed elsewhere [35]. Three cells were fabricated with commercial CGO scaffolds on both sides and sintered at 1250 °C for 2 h and one cell was prepared with mesoporous scaffolds on both sides and sintered at 900 °C for 5 h. Mesoporous $Ce_{0.8}Gd_{0.2}O_{1.9}$ powder employed in the CGO scaffold was synthesized as detailed elsewhere [28,33,34]. The obtained active area of the electrodes was $\approx$1.54 cm^2 ($\approx$1.4 cm diameter) in all cases.

The infiltration of the ceria scaffolds was automatically conducted by inkjet printing, using a customized printer, produced by Print3D Solutions (Albacete, Spain), which uses a commercial cartridge C6602A from Hewlett-Packard (Palo Alto, CA, USA) with a nozzle diameter $\approx$60 μm. The movement of the 3-axis system is controlled by Arduino (https://www.arduino.cc/, webpage consulted the 13 September 2021) and the printing process (with the C6602A cartridge) by Processing© (version 3.1.1, Processing Foundation, Brooklyn, NY, USA). The printing system (Figure S1) allows modification of the saturation parameter of the ink from 1 to 20. The saturation parameter corresponds to the distance between a deposited droplet and the next one, and therefore this is proportional to the amount of ink deposited in a single step [84]. After a first optimization with different saturation parameters, poor control of the process was observed for high saturation (i.e., 15/20 sat. and 20/20 sat.). Conversely, good injection was observed for lover values such as 5/20 sat. and 10/20 sat., and therefore the latter values were chosen as parameters for the functionalization of symmetrical scaffolds in the present study.

Using the described methodology, four symmetrical cells were fabricated and characterized. First, a reference cell without any infiltration (CGO) was fabricated and measured while another two were infiltrated keeping ink saturation at 5/20 sat. (5-CGO) and 10/20 sat. (10-CGO), respectively. Finally, a mesoporous CGO symmetrical cell was infiltrated with saturation at 10/20 sat. (10-CGO$_{meso}$). After infiltration, all the cells showed a total increase in mass of 25 $\pm$ 2 mg. Infiltration in all cases was separated in three different steps with a calcination treatment after each one at 500 °C for 30 min and a final thermal treatment at 800 °C for 3 h. The distance of the printing nozzles from the samples was $\approx$1 mm for all depositions. Since the 5-CGO cell was infiltrated with a lower saturation parameter (5/20 sat.) more depositions were necessary for each step in order to reach the same amount of infiltration solution in weight. In this manuscript, this deposition process is often referred as the "slow deposition process", and the process with saturation at 10/20 sat. is referred to as the "fast deposition process". The characteristics of the four different symmetrical test cells are reported in Table 1. A layer of commercial LSCF (Kceracell, Geumsan, Korea) powder was deposited on top of the scaffold of the four cells by airbrushing as current collector and sintered at 900 °C for 5 h.

Table 1. Characteristics of the cells produced. Commercial YSZ tape ($\approx$150 μm) was used for all the fabricated cells. A barrier layer made of commercial CGO decorated by Co oxide was deposited and sintered at 1275 °C. Commercial CGO scaffolds were sintered at 1250 °C and the mesoporous CGO at 900 °C.

CELL	Scaffold	Infiltration	Saturation
CGO	Commercial CGO	No	-
5-CGO	Commercial CGO	Yes	5/20 sat.
10-CGO	Commercial CGO	Yes	10/20 sat.
10-CGO$_{meso}$	Mesoporous CGO	Yes	10/20 sat.

2.4. Microstructural Characterization

Initial microstructural characterization of the obtained powders and cells was performed using a Carl ZEISS (Oberkochen, Germany) Auriga scanning electron microscope (SEM) equipped with an energy dispersive X-ray spectroscopy (EDX—X-Max, Oxford Instrument, Abingdon, UK) detector. The SEM-EDX characterization of the cells was conducted after electrochemical analysis. The crystalline phases were characterized by X-ray diffraction (XRD) θ–2θ (20 to 90°) measurements on a Bruker-D8 Advance equipment (Billerica, MA, USA) at room temperature using Cu-K_α radiation with a nickel filter and Lynx Eye detector. The mesoporous powders were also characterized using a Tristar II Brunauer–Emmett–Teller (BET) analyzer (Micromeritics, Norcross, GA, USA).

### 2.5. Electrochemical Characterization of Symmetrical Cells

Symmetrical cells were electrochemically characterized in a commercial ProboStatTM (NorECS AS, Oslo, Norway) station, inside a high-temperature vertical tubular furnace via impedance spectroscopy measurement (EIS—Novocontrol spectrometer by NOVOCONTROL Technologies GmbH & Co. KG, Bad Wildbad Baden Württemberg, Germany) from 900 to 600 °C (50 °C steps) and at synthetic air atmosphere. Gold paste (Fuelcellmaterials, Lewis Center, OH, USA) and meshes (Fiaxell Sarl, Lausanne, Switzerland) were used to ensure the current collection. The impedance measurements were conducted in potentiostatic mode from 10 to 100 mHz and an amplitude of 50 mV. Zview software (version 2.1, Southern Pines, NC, USA) was used to fit the impedance spectra.

3. Results and Discussion

3.1. Fabrication of the Symmetrical Cells

To ensure proper infiltration of LSCF inside the CGO scaffolds, the printability of formulated inks was evaluated. More specifically, the viscosity (Figure 1a) and the surface tension (Figure 1b) of the LSCF ink were measured to quantitatively determine suitability for inkjet printing [59,71,85]. After preliminary optimization (not showed here for the sake of clarity), LSCF infiltration ink presents a viscosity of 3.2 ± 0.1 mPa s and a surface tension of 33.1 ± 0.3 mN m^{-1}. The viscosity shows typical Newtonian behavior, maintaining a constant value for the explored share rate range. The measured surface tension is very stable with time, which means that the evaporation rate of the solution is slow. The resulting Z number was calculated as 14.0 ± 0.4. This value of Z indicates good printability as recently discussed by Liu and Derby, who fixed the printability region at $1 < Z < 20$ [71]. Further, Figure 1c shows the *We–Ca* plot (*We* number vs. the capillarity, *Ca*, of the suspension [86]) of the same ink, to provide a more exhaustive representation of its features. Since the jetting speed of the droplets produced by the HP C66002 could not be measured, *We* and *Ca* number ranges were estimated considering at a reasonable speed range from 1 to 10 m s^{-1} (black stars in the plot) [61,87]. It can be observed that at the considered speed range, the formulated LSCF ink overlaps the "printable" and the "satellite drops formation" areas. The formation of satellite drops is not considered an issue for the specific application of the infiltration and, during the printing process, no jetting issues were observed, experimentally confirming that the ink has good printability.

After optimization, the LSFC infiltration ink was printed on the pre-sintered CGO scaffolds. Then, the electrode layer was calcined at a low temperature (800 °C for 2 h) to crystallize the desired LSCF phase. Figure 2a–c show pictures of 5-CGO, 10-CGO and 10-CGO$_{meso}$ samples (after calcination). The deposited layer of the 5-CGO cell seems generally less homogeneous compared with that of 10-CGO and of 10-CGO$_{meso}$, which conversely demonstrate reasonable shaping and good homogeneity of the printed layer. XRD of the infiltrated electrode layers was carried out to investigate the crystallization and the reactivity of the LSCF perovskite. Figure 2d shows the XRD patterns of the 5-CGO, 10-CGO and 10-CGO$_{meso}$ samples. All the observed reflections can be fully indexed with the YSZ, CGO and LSCF diffraction patterns, indicating the formation of the desired perovskite phase and the absence of secondary phases [88–90].
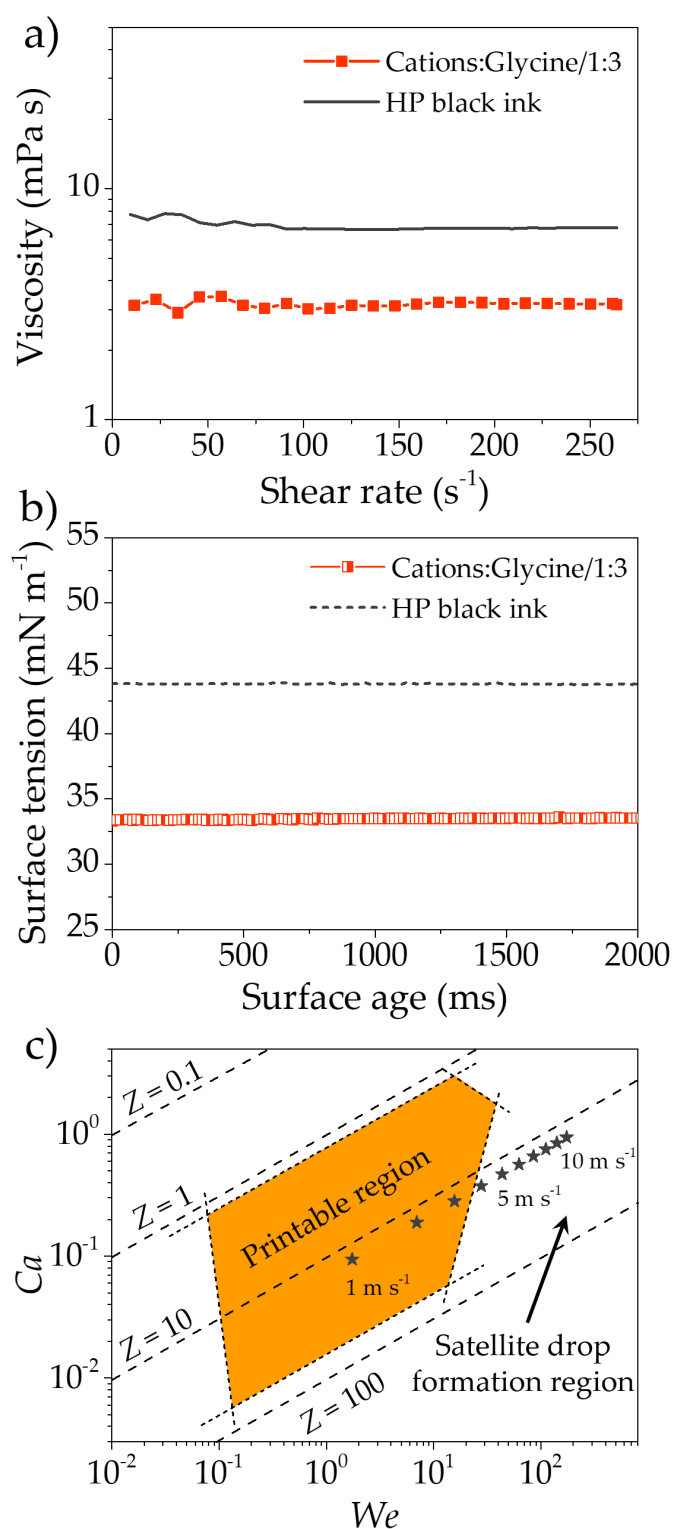
Figure 1. Viscosity (**a**) and surface tension (**b**) measurements of the sol-gel ink compared with the HP ink inside the cartridges [86]. (**c**) Printable region for IPJ deposition. The black stars represent the formulated ink considering the velocity range of the drops (1–10 m s^{-1}). The ink is between the preferable region for jetting and the satellite drop region. Panel (**c**) was adapted with permission from H. C. Nallan, J. A. Sadie, R. Kitsomboonloha, S. K. Volkman, and V. Subramanian, Langmuir 30, 13470 (2014). Copyright 2014 American Chemical Society.
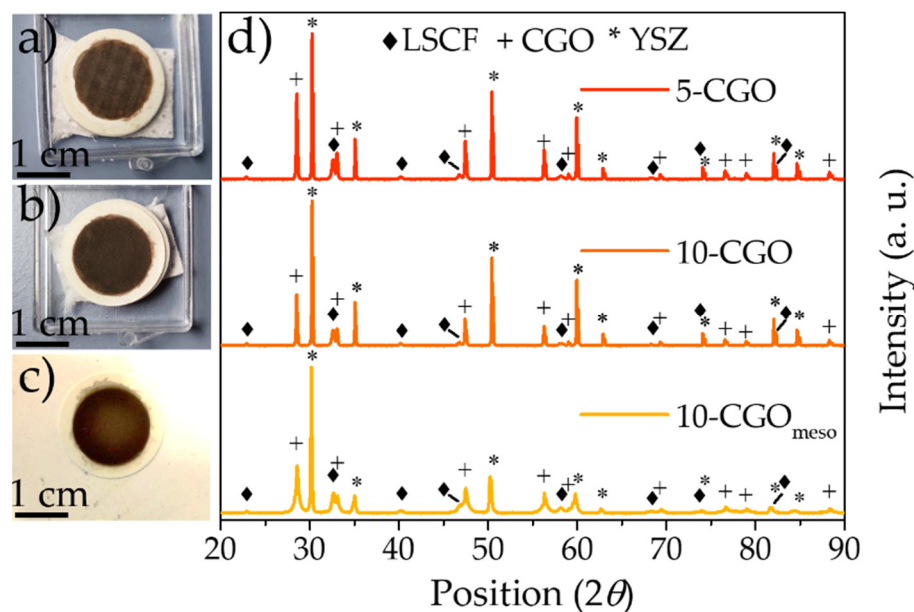
Figure 2. Digital pictures of the 5-CGO (**a**), 10-CGO (**b**) and 10-CGO$_{meso}$ (**c**) cells. XRD of the 5-CGO,10-CGO and 10-CGO$_{meso}$ cells after the infiltration and calcination of the LSCF solution (**d**). The presence of the LSCF characteristic peaks confirms the formation of the perovskite after the calcination process.

Microstructural characterization of the electrode cross sections was achieved through SEM on the four cells, after the electrochemical analysis of the following section, to observe the difference in morphology due to the variations in infiltration. Figure 3 shows SEM micrographs of the four cells presenting the general microstructure features of the obtained electrodes. Observing the micrographs one can immediately recognize the common structure for the CGO (Figure 3a), 5-CGO (Figure 3b), 10-CGO (Figure 3c) and 10-CGO$_{meso}$ (Figure 3d) cells. This structure consists of a YSZ electrolyte, a CGO barrier layer, a CGO scaffold infiltrated by LSCF in the case of 5-CGO, 10-CGO and 10-CGO$_{meso}$, and a LSCF layer airbrushed with commercial powder. A top layer of gold paste used as a current collector during electrochemical characterization, presented in the following section of the manuscript, can also be observed. The four electrodes present good attachment to the CGO barrier layer. Despite the good results of PLD barrier layers proposed by Morales et al. [15], the sprayed CGO barrier layers presented in this work show lower densification upon sintering. A certain level of porosity is typical for the current SoA deposition techniques (i.e., spray coating and screen printing) [14]. However, the densification of the layer does not represent an issue in the case of the present study, where no long-term characterization was conducted and a low fabrication temperature (900 °C) is applied. Generally, the four electrodes present a similar structure with good porosity that allows LSCF infiltration to impregnate the CGO scaffold.

Figure 4 shows SEM micrographs at a high magnification of 10-CGO (Figure 4a,b) and 10-CGO$_{meso}$ (Figure 4c,d) cells. The 10-CGO cell shows well-sintered coarsened particles with a reasonable but low porosity, while the scaffold of the 10-CGO$_{meso}$ retains the presence of the mesoporous structure even after thermal treatment (although one can notice a clear evolution of the ordered structure during the thermal treatment with respect to the synthesized mesoporous powders shown in Supplementary Info Figure S2). These microstructural variations are mainly due to the nature of the original powder and the different sintering temperature of both 10-CGO and 10-CGO$_{meso}$, which were treated at 1250 and 900 °C, respectively [33,91]. Because of the presence of the residual mesoporosity, the scaffold of the 10-CGO$_{meso}$ cell offers more active area for chemical reactions. This, combined with the infiltration of the LSCF phase is expected to increase the TPB of the

electrode. Moreover, the interconnected mesoporosity should improve the gas distribution and the thermal distribution of the functionalized electrode [31].
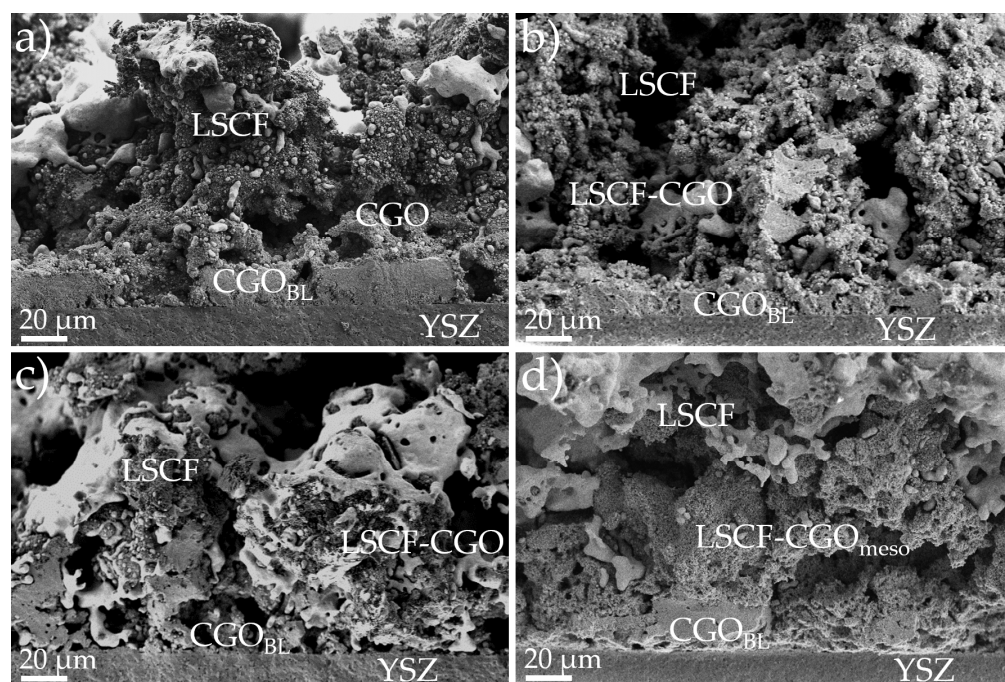

Figure 3. Cross-sectional SEM micrographs of the four different cells. (**a**) Micrograph of the CGO cell, fabricated with no infiltration. (**b**) Micrograph of the cell fabricated with slow infiltration and 5/20 sat. (5-CGO). (**c**) Micrograph of the cell fabricated with fast infiltration and 10/20 sat. (10-CGO). (**d**) Micrograph of the cell fabricated with a mesoporous CGO scaffold and fast infiltration (10-CGO$_{meso}$).
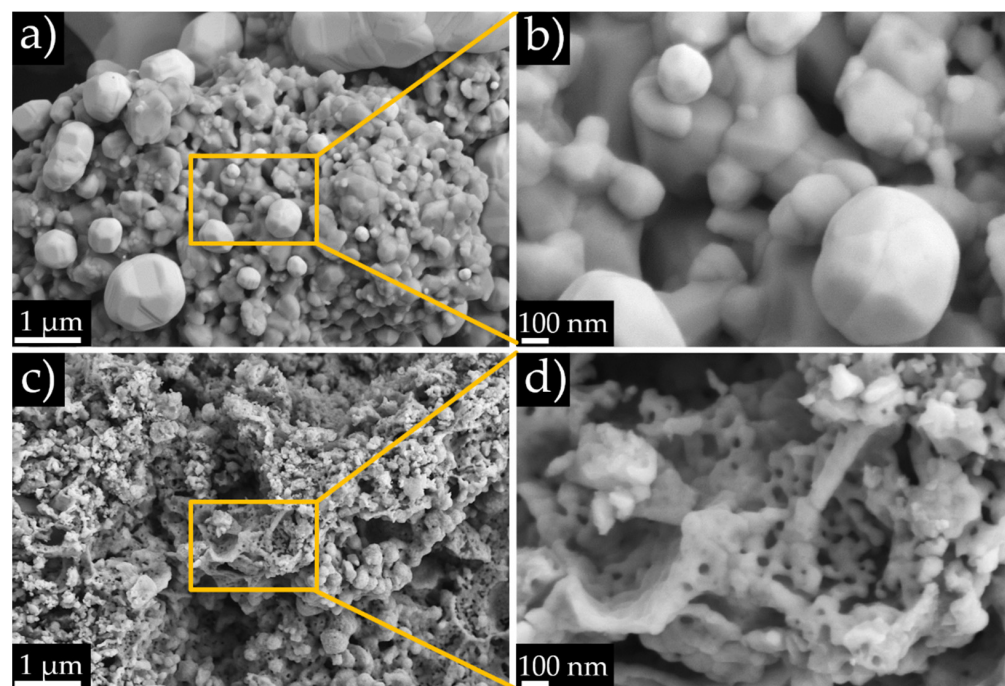
Figure 4. Representative region of the scaffold of the 10-CGO cell (**a**). SEM micrograph at a higher magnification (**b**). Representative region of the infiltrated scaffold of the 10-CGO$_{meso}$ cell (**c**). SEM micrograph at a higher magnification (**d**) where the residual mesoporosity can be observed.

Figure 5 shows SEM images of the reference (CGO) and infiltrated cells (5-CGO, 10-CGO and 10-CGO$_{meso}$). Regarding chemical composition, an SEM-EDX map of the reference cell (without infiltration) is presented in Figure 5a,b showing clear separation between the CGO scaffold (Ce signal in blue) and the LSCF current collector (La signal in red). A similar pattern is observed for 5-CGO in Figure 5c,d, suggesting poor infiltration of LSCF inside the CGO backbone under this infiltration condition. The amount of infiltrated LSCF clearly increases for 10-CGO and 10-CGO$_{meso}$ (Figure 5e–h). This means that faster infiltration with higher saturation is highly beneficial even for mesoporous scaffolds. Although the total amount of deposited material is similar in all cases (see Experimental section), it has been observed that the slower deposition process (made in more steps with drying at room temperature after each one) likely causes the progressive obstruction of the top part of the scaffold, blocking the infiltration in subsequent steps. This can be well observed analyzing the obtained linescans, which show very little LSCF in the region of the CGO scaffold of the 5-CGO cell, especially close to the electrolyte–electrode interface, where the ORRs are required. Conversely, good penetration of the LSCF phase inside the CGO scaffold in the case of the 10-CGO and 10-CGO$_{meso}$ cells with the fast process has been demonstrated. These results show better functionalization of the scaffold compared with traditional infiltration via micropipette injection reported in previous work of the group [35,37].
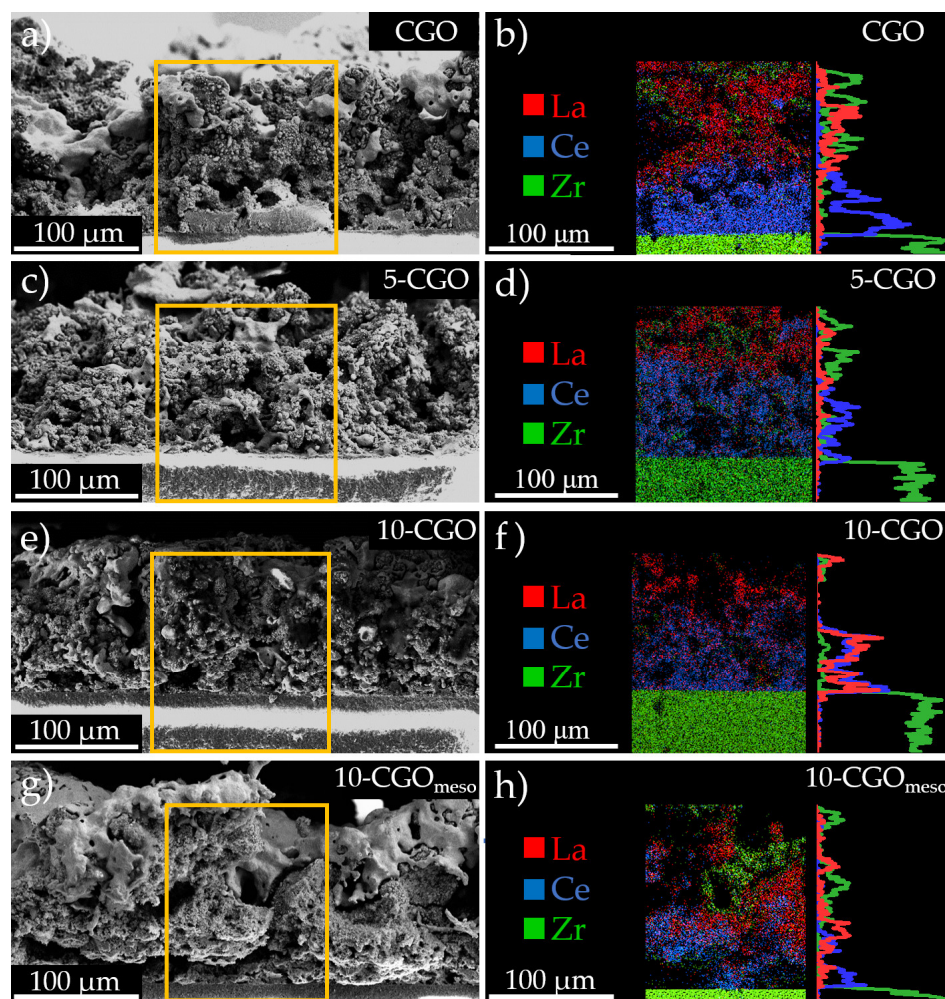
Figure 5. Representative SEM micrographs and EDX elemental maps of the CGO cell (panels (**a**,**b**)), the 5-CGO cell (panels (**c**,**d**)), the 10-CGO cell (panels (**e**,**f**)) and the 10-CGO$_{meso}$ cell (panels (**g**,**h**). In all the EDX maps, the YSZ, CGO and LSCF phases are indicated by their main representative element. Zr (green), Ce (blue) and La (red) show the presence of YSZ, CGO and LSCF, respectively.

3.2. Electrochemical Characterization of the Infiltrated Cells

The complete set of samples (CGO, 5-CGO, 10-CGO and 10-CGO$_{meso}$) were characterized under symmetrical configuration by electrochemical impedance spectroscopy (Figure 6). Figure 6a shows the resulting impedance spectra of the reference cell 5-CGO tested at three different temperatures, 700, 750 and 800 °C, which are the typical operating temperatures for SOC devices with similar electrodes. Each impedance spectrum was successfully fitted applying the equivalent circuit shown in Figure 6a. This circuit, the simplest circuit able to fit the asymmetric impedance spectra, is composed by an inductance L, a serial resistance R_s and two ZARC elements. R_s can be easily assigned to resistance contributions in series, mainly dominated by the electrolyte, while the combination of the resistance of the ZARC elements gives the total polarization resistance associated with the symmetrical electrodes ($R_{pol} = R_1 + R_2$). In order to compare samples with different levels of infiltration, the impedance spectra of the four cells at a fixed temperature of 750 °C were plotted in Figure 6b. One can immediately notice the difference in terms of overall area-specific resistance ($ASR = (R_s + R_{pol}) \times A$, where A is the area of the cell) of the four cells due to infiltration. The reference CGO cell presents an overall ASR of $\approx$5.3 Ω cm^2, while a progressive decrease in this value is observed as a function of the deeper functionalization of the scaffold. The obtained ASR values for 5-CGO, 10-CGO and 10-CGO$_{meso}$ samples were $\approx$2.9, $\approx$1.8 and $\approx$1.2 Ω cm^2, respectively. Slower infiltration of LSCF inside the scaffold (5-CGO) reduces to almost half the overall resistance, compared to the reference value for the CGO cell. Faster infiltrated samples (10-CGO) divide the overall resistance of the reference value by a factor of three or four (with or without the mesoporous scaffold, respectively). The 10-CGO$_{meso}$ cell presents the lowest measured ASR, $\approx$1.2 Ω cm^2 at 750 °C. Considering electrodes with a similar composition, Sanna et al. reported an ASR of $\approx$2.8 Ω cm^2 at the same temperature [92]. Conversely, Nielsen et al. reported an ASR of $\approx$0.34 Ω cm^2 at the same temperature [93]. Considering only the contribution of the LSCF–CGO electrode (ASR_{pol}) of the 10-CGO$_{meso}$ cell, the value decreases to $\approx$0.18 Ω cm^2, much closer to the 0.1 Ω cm^2 measured by Nielsen et al. for their LSCF–CGO composite electrode [93]. The considerable ohmic contribution (ASR_s) observed even for 10-CGO$_{meso}$ cell ($\approx$0.8 Ω cm^2) could also be due to the airbrushed CGO barrier layer, deposited on top of the YSZ electrode in order to avoid the formation of secondary phases with the Sr-rich perovskite during the sintering step. Localized barrier layer discontinuities are reported in the microstructural characterization section (Figure 3). As mentioned earlier, previous works of the group pointed out the better efficiency and the good morphology granted by alternative deposition techniques such as PLD for CGO barrier layers [15,36].

The plots of serial and polarization ASR as a function of the inverse of temperature are reported at between 600 and 900 °C in Figure 6c,d. Slightly higher activation energy values of the serial resistance are obtained for the CGO cell (0.97 $\pm$ 0.04 eV) compared to those measured for 5-CGO, 10-CGO and 10-CGO$_{meso}$ (0.93 $\pm$ 0.01, 0.92 $\pm$ 0.01 and 0.93 $\pm$ 0.02 eV, respectively). Despite both values being very close to that reported for the 8YSZ electrolyte [94], observed differences could be explained considering contributions to the serial resistance of both the electrolyte and the CGO scaffold [44,95]. The observed reduction in serial ASR values is likely related to a decrease in the CGO layer on the better infiltrated functional layers that improves the current collection of the cells (promoted by the homogeneous and continuous infiltration of the LSCF phase through the CGO scaffold).

Regarding the study of polarization resistance (Figure 6d), the activation energy range is from 1.2 to 1.4 eV, which is typical for LSCF–CGO composites previously reported in the literature [54]. Cells with a commercial CGO scaffold present similar values (1.23 $\pm$ 0.01, 1.23 $\pm$ 0.02 and 1.29 $\pm$ 0.01 eV for CGO, 5-CGO and 10-CGO cells, respectively) while a slight increase is observed employing the mesoporous scaffold (1.38 $\pm$ 0.04 eV). This difference could be caused by either the presence of small amounts of silica contamination ($\approx$1 wt%), due to the incomplete removal of the employed mesoporous template, or dopant segregation to the interfaces, as previously reported by the authors [36,96]. Concerning

ASR_{pol} values, a clear difference in resistance between scaffolds with and without infiltration is observed (due to the lack of a catalytic phase in the functional layer). Moreover, an increasing beneficial effect of infiltration is observed for higher saturation and the use of mesoporous CGO scaffolds, which implies a higher active area. Better LSCF distribution within the scaffold for 10-CGO (see Figure 5f,h) and the considerable increase in active area in 10-CGO$_{meso}$ (see Figure 4d) are straightforward arguments that justify better performance by extension of the TPB active region of the functional layer. Overall, as in the case of serial resistance, the combination of better infiltration a mesoporous microstructure improves the performance of the electrode significantly.
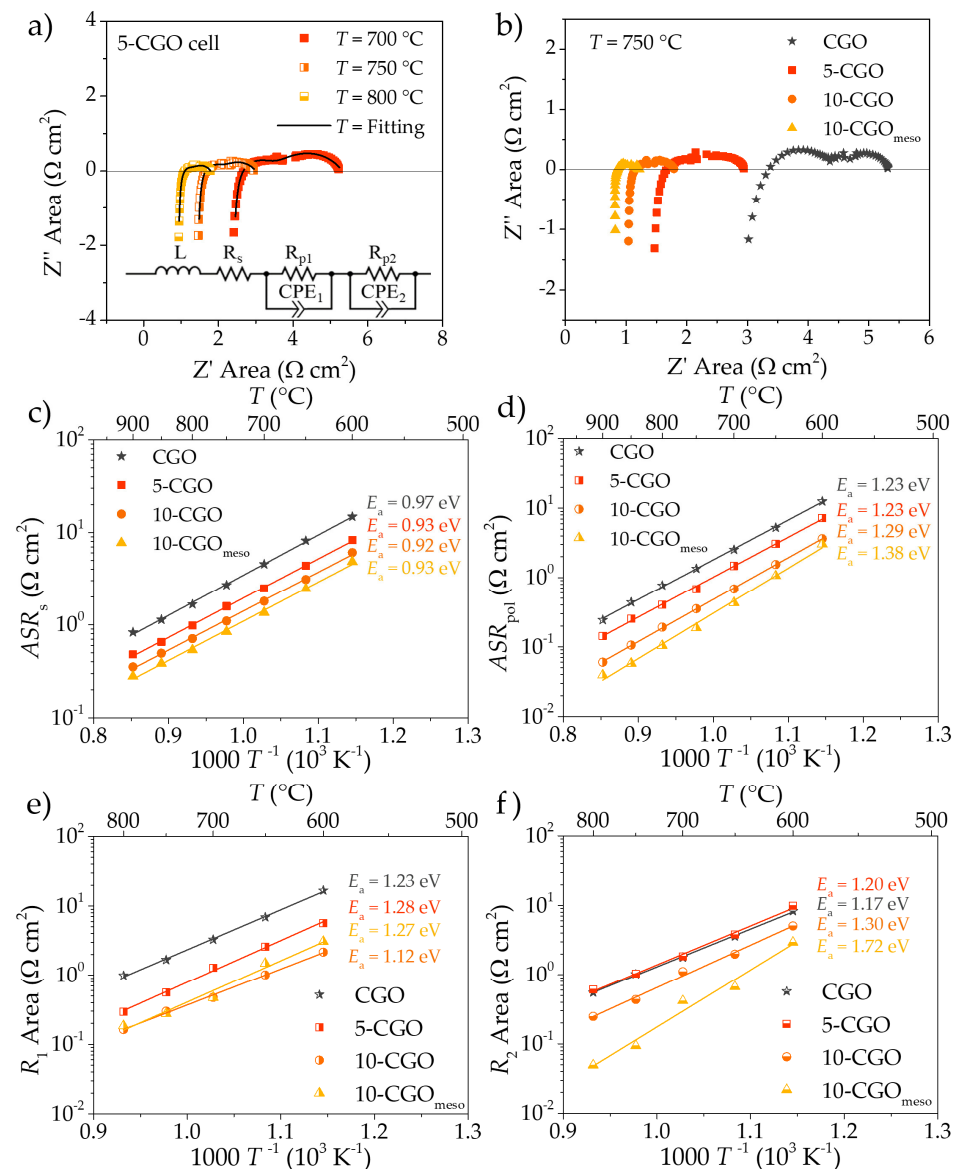
Figure 6. EIS spectra of the 5-CGO cell at 700, 750 and 800 °C. (**a**) The equivalent circuit used for the (**b**) EIS spectra of the four cells (CGO, 5-CGO, 10-CGO and 10-CGO$_{meso}$) at 750 °C. (**c**) Serial *ASR* contributions of CGO, 5-CGO, 10-CGO and 10-CGO$_{meso}$ cells as a function of the inverse of temperature. (**d**) Polarization *ASR* contributions of CGO, 5-CGO, 10-CGO and 10-CGO$_{meso}$ cells as a function of the inverse of temperature. The values were obtained by fitting with the equivalent circuit shown in (**a**). (**e**) R_1 and (**f**) R_2 of the two ZARC elements used for the fitting of the EIS spectra as a function of the inverse of temperature.

Figure 6e,f show the plots of the two contributions to the ASR_{pol} (R_1 and of R_2, respectively) as a function of the inverse of temperature. These contributions arise from the two ZARC elements present in the equivalent circuit shown in Figure 6a. Capacitance obtained from the fitting ranged from 1×10^{-6} to 5×10^{-3} F cm^{-2} for C_1, with a characteristic frequency in the range of 10^4–10^2 Hz, and from 5×10^{-4} to 5×10^{-2} F cm^{-2} for C_2, with a frequency within the range 10^1–10^0 Hz. Charge transfer phenomena are compatible with C_1 [46,57,97,98], while the larger values of C_2 are characteristic of surface exchange reactions such as the dissociation and adsorption of oxygen molecules [42,98,99]. In Supplementary Information (Section S3, Figure S3), the plots of C_1 vs. T and C_2 vs. T of the four cells are included for the sake of completeness. An observed increase in capacitance after infiltration (for both C_1 and C_2) is compatible with the increase in contact points between CGO and LSCF, as previously reported by dos Santos Gomez et al. for similar functionalization through infiltration [98]. Considering mesoporous CGO, this increase in the capacitance value was not observed for C_2 (Figure S3b), which is probably related again to the charge transfer blocking effect of SiO$_2$ impurities and dopant segregated to the surface of the mesoporous powder [100,101]. This hypothesis is compatible with ASR_{pol} behavior since R_1 remains similar for 10-CGO and 10-CGO$_{meso}$, which indicates a certain blocking effect of the charge transfer at the LSCF–CGO interfaces, while R_2 is notably improved for 10-CGO$_{meso}$, which indicates better performance for non-charge transfer phenomena taking place at the surface.

4. Conclusions

Composites layers of LSCF–CGO were successfully fabricated by automatic infiltration using DOD-IJP for their use as functional oxygen electrodes in solid oxide cells. Symmetrical electrochemical cells with infiltrated oxygen electrode functional layers (YSZ/LSCF–CGO/LSCF) were fabricated and measured in the present work. After optimization of the formulated LSCF ink, infiltration of different pre-sintered CGO scaffolds was successfully demonstrated. The optimization of the saturation parameter of the ink was critical to ensure the homogeneous infiltration of the porous backbones. Symmetrical cells with optimal infiltrated layers showed a minimum ASR of ≈ 1.2 Ω cm^2 at 750 °C, which is competitive with state-of-the-art results reported for composites of similar materials. Electrochemical impedance spectroscopy analysis carried out in this work concluded that optimization of the infiltration of the ceramic backbones reduces polarization resistance by improving the activity of the electrodes. Electrochemical characterization also highlighted the improvement in the serial contribution, due to better catalytic activity and current collection along the electrode. Moreover, CGO scaffolds fabricated by using mesoporous powders were successfully infiltrated, resulting in an even lower ASR_{pol}, ≈ 0.18 Ω cm^2 at 750 °C, due to an increase in the active area of the infiltrated backbone. Overall, this work confirms the recently reported good electrode infiltration in solid oxide cells and paves the way for automation of reproducible and scalable large-area infiltration based on ink jet printing technology.

Author Contributions: Conceptualization, S.A., F.B., M.T. and A.T.; formal analysis, S.A., L.M.-S., F.B., M.T. and A.T.; investigation, S.A. and L.M.-S.; supervision, F.B., M.T. and A.T.; visualization, S.A. and L.M.-S.; writing—original draft, S.A.; writing—review and editing, S.A., F.B., M.T. and A.T. All authors have read and agreed to the published version of the manuscript.

References

1. Brisse, A.; Schefold, J.; Zahid, M. High temperature water electrolysis in solid oxide cells. *Int. J. Hydrogen Energy* **2008**, *33*, 5375–5382. [CrossRef]
2. Hauch, A.; Ebbesen, S.D.; Jensen, S.H.; Mogensen, M. Highly efficient high temperature electrolysis. *J. Mater. Chem.* **2008**, *18*, 2331–2340. [CrossRef]
3. Laguna-Bercero, M.A. Recent advances in high temperature electrolysis using solid oxide fuel cells: A review. *J. Power Sources* **2012**, *203*, 4–16. [CrossRef]
4. Zheng, Y.; Wang, J.; Yu, B.; Zhang, W.; Chen, J.; Qiao, J.; Zhang, J. A review of high temperature co-electrolysis of H_2O and CO_2 to produce sustainable fuels using solid oxide electrolysis cells (SOECs): Advanced materials and technology. *Chem. Soc. Rev.* **2017**, *46*, 1427–1463. [CrossRef]
5. Stambouli, A.; Traversa, E. Solid oxide fuel cells (SOFCs): A review of an environmentally clean and efficient source of energy. *Renew. Sustain. Energy Rev.* **2002**, *6*, 433–455. [CrossRef]
6. Singhal, S.C.; Kendall, K. *High Temperature and Solid Oxide Fuel Cells: Fundamentals, Design and Applications*, 1st ed.; Elsevier: Hoboken, NJ, USA, 2003; Volume 16, ISBN 9781856173872.
7. Mahato, N.; Banerjee, A.; Gupta, A.; Omar, S.; Balani, K. Progress in material selection for solid oxide fuel cell technology: A review. *Prog. Mater. Sci.* **2015**, *72*, 141–337. [CrossRef]
8. Adler, S.B. Factors Governing Oxygen Reduction in Solid Oxide Fuel Cell Cathodes. *Chem. Rev.* **2004**, *104*, 4791–4844. [CrossRef]
9. Irvine, J.T.S.; Neagu, D.; Verbraeken, M.C.; Chatzichristodoulou, C.; Graves, C.R.; Mogensen, M.B. Evolution of the electrochemical interface in high-temperature fuel cells and electrolysers. *Nat. Energy* **2016**, *1*, 15014. [CrossRef]
10. Connor, P.A.; Yue, X.; Savaniu, C.D.; Price, R.; Triantafyllou, G.; Cassidy, M.; Kerherve, G.; Payne, D.J.; Maher, R.C.; Cohen, L.; et al. Tailoring SOFC Electrode Microstructures for Improved Performance. *Adv. Energy Mater.* **2018**, *8*. [CrossRef]
11. Zhang, H.; Zhao, F.; Chen, F.; Xia, C. Nano-structured $Sm_{0.5}Sr_{0.5}CoO_{3-\delta}$ electrodes for intermediate-temperature SOFCs with zirconia electrolytes. *Solid State Ionics* **2011**, *192*, 591–594. [CrossRef]
12. Park, H.J.; Park, J.Y. A promising high-performance lanthanum ferrite-based composite cathode for intermediate temperature solid oxide fuel cells. *Solid State Ionics* **2013**, *244*, 30–34. [CrossRef]
13. Torrell, M.; Morata, A.; Kayser, P.; Kendall, M.; Tarancón, A. Performance and long term degradation of 7 W micro-tubular solid oxide fuel cells for portable applications. *J. Power Sources* **2015**, *285*, 439–448. [CrossRef]
14. Morales, M.; Miguel-Pérez, V.; Tarancon, A.; Slodczyk, A.; Torrell, M.; Ballesteros, B.; Ouweltjes, J.; Bassat, J.; Montinaro, D.; Morata, A. Multi-scale analysis of the diffusion barrier layer of gadolinia-doped ceria in a solid oxide fuel cell operated in a stack for 3000 h. *J. Power Sources* **2017**, *344*, 141–151. [CrossRef]
15. Morales, M.; Pesce, A.; Slodczyk, A.; Torrell, M.; Piccardo, P.; Montinaro, D.; Tarancón, A.; Morata, A. Enhanced Performance of Gadolinia-Doped Ceria Diffusion Barrier Layers Fabricated by Pulsed Laser Deposition for Large-Area Solid Oxide Fuel Cells. *ACS Appl. Energy Mater.* **2018**, *1*, 1955–1964. [CrossRef]
16. Vohs, J.M.; Gorte, R.J. High-Performance SOFC Cathodes Prepared by Infiltration. *Adv. Mater.* **2009**, *21*, 943–956. [CrossRef]
17. Jiang, S.P. Nanoscale and nano-structured electrodes of solid oxide fuel cells by infiltration: Advances and challenges. *Int. J. Hydrogen Energy* **2012**, *37*, 449–470. [CrossRef]
18. Ding, D.; Li, X.; Lai, S.Y.; Gerdes, K.; Liu, M. Enhancing SOFC cathode performance by surface modification through infiltration. *Energy Environ. Sci.* **2013**, *7*, 552–575. [CrossRef]
19. Shah, M.; Barnett, S. Solid oxide fuel cell cathodes by infiltration of $La_{0.6}Sr_{0.4}Co_{0.2}Fe_{0.8}O_{3-\delta}$ into Gd-Doped Ceria. *Solid State Ionics* **2008**, *179*, 2059–2064. [CrossRef]
20. Sholklapper, T.Z.; Jacobson, C.P.; Visco, S.J.; De Jonghe, L.C. Synthesis of Dispersed and Contiguous Nanoparticles in Solid Oxide Fuel Cell Electrodes. *Fuel Cells* **2008**, *8*, 303–312. [CrossRef]
21. Sun, C.; Li, H.; Chen, L. Nanostructured ceria-based materials: Synthesis, properties, and applications. *Energy Environ. Sci.* **2012**, *5*, 8475–8505. [CrossRef]
22. Sun, C.; Sun, J.; Xiao, G.; Zhang, H.; Qiu, X.; Li, H.; Chen, L. Mesoscale Organization of Nearly Monodisperse Flowerlike Ceria Microspheres. *J. Phys. Chem. B* **2006**, *110*, 13445–13452. [CrossRef]

23. Sun, C.; Li, H.; Chen, L. Study of flowerlike CeO_2 microspheres used as catalyst supports for CO oxidation reaction. *J. Phys. Chem. Solids* **2007**, *68*, 1785–1790. [CrossRef]

24. Sun, C.; Xie, Z.; Xia, C.; Li, H.; Chen, L. Investigations of mesoporous CeO_2–Ru as a reforming catalyst layer for solid oxide fuel cells. *Electrochem. Commun.* **2006**, *8*, 833–838. [CrossRef]

25. Mamak, M.; Coombs, A.N.; Ozin, G. Self-Assembling Solid Oxide Fuel Cell Materials: Mesoporous Yttria-Zirconia and Metal-Yttria-Zirconia Solid Solutions. *J. Am. Chem. Soc.* **2000**, *122*, 8932–8939. [CrossRef]

26. Mamak, M.; Coombs, A.N.; Ozin, G.A. Mesoporous Nickel–Yttria–Zirconia Fuel Cell Materials. *Chem. Mater.* **2001**, *13*, 3564–3570. [CrossRef]

27. Serra, J.M.; Uhlenbruck, S.; Meulenberg, W.A.; Buchkremer, H.P.; Stöver, D. Nano-structuring of solid oxide fuel cells cathodes. *Top. Catal.* **2006**, *40*, 123–131. [CrossRef]

28. Almar, L.; Andreu, T.; Morata, A.; Tarancon, A. Mesoporous NiO-CGO Obtained by Hard Template as High Surface Area Anode for IT-SOFC. *ECS Trans.* **2011**, *35*, 1647–1654. [CrossRef]

29. Almar, L.; Morata, A.; Torrell, M.; Gong, M.; Andreu, T.; Liu, M.; Tarancón, A. A Durable Electrode for Solid Oxide Cells: Mesoporous Ce0.8Sm0.2O1.9 Scaffolds Infiltrated with a $Sm_{0.5}Sr_{0.5}CoO_{3-\delta}$ Catalyst. *Electrochim. Acta* **2017**, *235*, 646–653. [CrossRef]

30. Laha, S.C.; Ryoo, R. Synthesis of thermally stable mesoporous cerium oxide with nanocrystalline frameworks using mesoporous silica templates. *Chem. Commun.* **2003**, 2138–2139. [CrossRef] [PubMed]

31. Almar, L.; Morata, A.; Torrell, M.; Gong, M.; Liu, M.; Andreu, T.; Tarancón, A. Synthesis and characterization of robust, mesoporous electrodes for solid oxide fuel cells. *J. Mater. Chem. A* **2016**, *4*, 7650–7657. [CrossRef]

32. Yang, H.; Zhao, D. Synthesis of replica mesostructures by the nanocasting strategy. *J. Mater. Chem.* **2005**, *15*, 1217–1231. [CrossRef]

33. Almar, L.; Andreu, T.; Morata, A.; Torrell, M.; Yedra, L.; Estradé, S.; Peiró, F.; Tarancón, A. High-surface-area ordered mesoporous oxides for continuous operation in high temperature energy applications. *J. Mater. Chem. A* **2013**, *2*, 3134–3141. [CrossRef]

34. Torrell, M.; Almar, L.; Morata, A.; Tarancón, A. Synthesis of mesoporous nanocomposites for their application in solid oxide electrolysers cells: Microstructural and electrochemical characterization. *Faraday Discuss.* **2015**, *182*, 423–435. [CrossRef]

35. Hernández, E.; Baiutti, F.; Morata, A.; Torrell, M.; Tarancón, A. Infiltrated mesoporous oxygen electrodes for high temperature co-electrolysis of H2O and CO2 in solid oxide electrolysis cells. *J. Mater. Chem. A* **2018**, *6*, 9699–9707. [CrossRef]

36. Anelli, S.; Baiutti, F.; Hornés, A.; Bernadet, L.; Torrell, M.; Tarancón, A. Improved mesostructured oxygen electrodes for highly performing solid oxide cells for co-electrolysis of steam and carbon dioxide. *J. Mater. Chem. A* **2019**, *7*, 27458–27468. [CrossRef]

37. Anelli, S.; Hernández, E.; Bernadet, L.; Sun, X.; Hagen, A.; Baiutti, F.; Torrell, M.; Tarancón, A. Co-electrolysis of steam and carbon dioxide in large area solid oxide cells based on infiltrated mesoporous oxygen electrodes. *J. Power Sources* **2020**, *478*, 228774. [CrossRef]

38. Hedayat, N.; Du, Y.; Ilkhani, H. Review on fabrication techniques for porous electrodes of solid oxide fuel cells by sacrificial template methods. *Renew. Sustain. Energy Rev.* **2017**, *77*, 1221–1239. [CrossRef]

39. Wan, Y.; Zhao, D. On the Controllable Soft-Templating Approach to Mesoporous Silicates. *Chem. Rev.* **2007**, *107*, 2821–2860. [CrossRef] [PubMed]

40. Peng, L.; Zhang, J.; Xue, Z.; Han, B.; Sang, X.; Liu, C.; Yang, G. Highly mesoporous metal–organic framework assembled in a switchable solvent. *Nat. Commun.* **2014**, *5*, 4465. [CrossRef] [PubMed]

41. Deng, X.; Chen, K.; Tüysüz, H. Protocol for the Nanocasting Method: Preparation of Ordered Mesoporous Metal Oxides. *Chem. Mater.* **2016**, *29*, 40–52. [CrossRef]

42. Nie, L.; Liu, M.; Zhang, Y.; Liu, M. $La_{0.6}Sr_{0.4}Co_{0.2}Fe_{0.8}O_{3-\delta}$ cathodes infiltrated with samarium-doped cerium oxide for solid oxide fuel cells. *J. Power Sources* **2010**, *195*, 4704–4708. [CrossRef]

43. Wang, F.; Chen, D.; Shao, Z. $Sm_{0.5}Sr_{0.5}CoO_{3-\delta}$-infiltrated cathodes for solid oxide fuel cells with improved oxygen reduction activity and stability. *J. Power Sources* **2012**, *216*, 208–215. [CrossRef]

44. Fan, H.; Keane, M.; Li, N.; Tang, D.; Singh, P.; Han, M. Electrochemical stability of $La_{0.6}Sr_{0.4}Co_{0.2}Fe_{0.8}O_{3-\delta}$-infiltrated YSZ oxygen electrode for reversible solid oxide fuel cells. *Int. J. Hydrogen Energy* **2014**, *39*, 14071–14078. [CrossRef]

45. Fan, H.; Han, M. Electrochemical stability of $Sm_{0.5}Sr_{0.5}CoO_{3-\delta}$ infiltrated YSZ for solid oxide fuel cells or electrolysis cells. *Faraday Discuss.* **2015**, *182*, 477–491. [CrossRef]

46. Burye, T.E.; Nicholas, J. Nano-ceria pre-infiltration improves $La_{0.6}Sr_{0.4}Co_{0.8}Fe_{0.2}O_{3-x}$ infiltrated Solid Oxide Fuel Cell cathode performance. *J. Power Sources* **2015**, *300*, 402–412. [CrossRef]

47. Fan, H.; Zhang, Y.; Han, M. Infiltration of $La_{0.6}Sr_{0.4}FeO_{3-\delta}$ nanoparticles into YSZ scaffold for solid oxide fuel cell and solid oxide electrolysis cell. *J. Alloys Compd.* **2017**, *723*, 620–626. [CrossRef]

48. Skafte, T.L.; Hjelm, J.; Blennow, P.; Graves, C.R. Reactivating the Ni-YSZ electrode in solid oxide cells and stacks by infiltration. *J. Power Sources* **2018**, *378*, 685–690. [CrossRef]

49. Tong, X.; Ovtar, S.; Brodersen, K.; Hendriksen, P.V.; Chen, M. Large-area solid oxide cells with $La_{0.6}Sr_{0.4}CoO_{3-\delta}$ infiltrated oxygen electrodes for electricity generation and hydrogen production. *J. Power Sources* **2020**, *451*, 227742. [CrossRef]

50. Hong, J.; Balamurugan, C.; Im, H.-N.; Jeon, S.-Y.; Yoo, Y.-S.; Song, S.-J. The Electrochemical Properties of Nanocrystalline $Gd_{0.1}Ce_{0.9}O_{1.95}$ Infiltrated Solid Oxide Co-Electrolysis Cells. *J. Electrochem. Soc.* **2018**, *165*, F132–F141. [CrossRef]

51. Ovtar, S.; Hauch, A.; Veltzé, S.; Chen, M. Comparison between $La_{0.6}Sr_{0.4}CoO_{3-d}$ and $LaNi_{0.6}Co_{0.4}O_{3-d}$ infiltrated oxygen electrodes for long-term durable solid oxide fuel cells. *Electrochim. Acta* **2018**, *266*, 293–304. [CrossRef]

52. Tomov, R.I.; Fakeeh, A.; Krishnan, V.V.; Balasubramanian, K.; Kumar, V.R.; Glowacki, B.A. Direct Ceramic Inkjet Printing and Infiltration of Functional Coatings for Metal Supported SOFC. *ECS Trans.* **2015**, *68*, 2491–2501. [CrossRef]

53. Tomov, R.I.; Duncan, R.; Krauz, M.; Glowacki, B.A.; Kumar, R.V.; Filipowicz, M.; Dudek, M.; Olkuski, T.; Styszko, K. Inkjet printing and inkjet infiltration of functional coatings for SOFCs fabrication. *E3S Web Conf.* **2016**, *10*, 98. [CrossRef]

54. Tomov, R.I.; Mitchell-Williams, T.; Gao, C.; Kumar, R.V.; Glowacki, B.A. Performance optimization of LSCF/Gd:CeO$_2$ composite cathodes via single-step inkjet printing infiltration. *J. Appl. Electrochem.* **2017**, *47*, 641–651. [CrossRef] [PubMed]

55. Mitchell-Williams, T.B.; Tomov, R.I.; Saadabadi, S.A.; Krauz, M.; Aravind, P.V.; Glowacki, B.A.; Kumar, R.V. Infiltration of commercially available, anode supported SOFC's via inkjet printing. *Mater. Renew. Sustain. Energy* **2017**, *6*, 1–9. [CrossRef]

56. Wang, C.; Tomov, R.I.; Glowacki, B.A.; Mitchell-Williams, T.B.; Kumar, R.V.; Glowacki, B.A. Inkjet printing infiltration of Ni-Gd:CeO$_2$ anodes for low temperature solid oxide fuel cells. *J. Appl. Electrochem.* **2017**, *47*, 1227–1238. [CrossRef]

57. Tomov, R.I.; Mitchel-Williams, T.B.; Maher, R.; Kerherve, G.; Cohen, L.; Payne, D.J.; Kumar, R.V.; Glowacki, B.A. The synergistic effect of cobalt oxide and Gd-CeO$_2$ dual infiltration in LSCF/CGO cathodes. *J. Mater. Chem. A* **2018**, *6*, 5071–5081. [CrossRef]

58. Venezia, E.; Viviani, M.; Presto, S.; Kumar, R.V.; Tomov, R.I. Inkjet Printing Functionalization of SOFC LSCF Cathodes. *Nanomaterials* **2019**, *9*, 654. [CrossRef]

59. Derby, B. Inkjet Printing of Functional and Structural Materials: Fluid Property Requirements, Feature Stability, and Resolution. *Annu. Rev. Mater. Res.* **2010**, *40*, 395–414. [CrossRef]

60. Derby, B. Additive Manufacture of Ceramics Components by Inkjet Printing. *Engineering* **2015**, *1*, 113–123. [CrossRef]

61. Hoath, S.D. *Fundamentals of Inkjet Printing: The Science of Inkjet and Droplets*; John Wiley & Sons: Weinheim, Germany, 2016; Volume 1, ISBN 9783527684724.

62. Yin, Z.; Huang, Y.; Bu, N.; Wang, X.; Xiong, Y. Inkjet printing for flexible electronics: Materials, processes and equipments. *Chin. Sci. Bull.* **2010**, *55*, 3383–3407. [CrossRef]

63. Sachs, E.; Cima, M.; Williams, P.; Brancazio, D.; Cornie, J. Three Dimensional Printing: Rapid Tooling and Prototypes Directly from a CAD Model. *J. Eng. Ind.* **1992**, *114*, 481–488. [CrossRef]

64. Bietsch, A.; Zhang, J.; Hegner, M.; Lang, H.P.; Gerber, C. Rapid functionalization of cantilever array sensors by inkjet printing. *Nanotechnology* **2004**, *15*, 873–880. [CrossRef]

65. Fasaki, I.; Siamos, K.; Arin, M.; Lommens, P.; Van Driessche, I.; Hopkins, S.; Glowacki, B.; Arabatzis, I. Ultrasound assisted preparation of stable water-based nanocrystalline TiO2 suspensions for photocatalytic applications of inkjet-printed films. *Appl. Catal. A Gen.* **2012**, *411–412*, 60–69. [CrossRef]

66. Farandos, N.; Li, T.; Kelsall, G. 3-D inkjet-printed solid oxide electrochemical reactors. II. LSM-YSZ electrodes. *Electrochim. Acta* **2018**, *270*, 264–273. [CrossRef]

67. Feng, Z.; Liu, L.; Li, L.; Chen, J.; Liu, Y.; Li, Y.; Hao, L.; Wu, Y. 3D printed Sm-doped ceria composite electrolyte membrane for low temperature solid oxide fuel cells. *Int. J. Hydrogen Energy* **2019**, *44*, 13843–13851. [CrossRef]

68. Atkinson, A.; Doorbar, J.; Hudd, A.; Segal, D.L.; White, P.J. Continuous ink-jet printing using sol-gel "Ceramic" inks. *J. Sol-Gel Sci. Technol.* **1997**, *8*, 1093–1097. [CrossRef]

69. Teng, W.D.; Edirisinghe, M.J. Development of Ceramic Inks for Direct Continuous Jet Printing. *J. Am. Ceram. Soc.* **2005**, *81*, 1033–1036. [CrossRef]

70. Tomov, R.; Krauz, M.; Jewulski, J.; Hopkins, S.; Kluczowski, J.; Glowacka, D.; Glowacki, B. Direct ceramic inkjet printing of yttria-stabilized zirconia electrolyte layers for anode-supported solid oxide fuel cells. *J. Power Sources* **2010**, *195*, 7160–7167. [CrossRef]

71. Liu, Y.; Derby, B. Experimental study of the parameters for stable drop-on-demand inkjet performance. *Phys. Fluids* **2019**, *31*, 032004. [CrossRef]

72. Farandos, N.; Kleiminger, L.; Li, T.; Hankin, A.; Kelsall, G. Three-dimensional Inkjet Printed Solid Oxide Electrochemical Reactors. I. Yttria-stabilized Zirconia Electrolyte. *Electrochim. Acta* **2016**, *213*, 324–331. [CrossRef]

73. Liu, X.; Tarn, T.-J.; Huang, F.; Fan, J. Recent advances in inkjet printing synthesis of functional metal oxides. *Particuology* **2015**, *19*, 1–13. [CrossRef]

74. Zhong, Y.; Fang, H.; Ma, Q.; Dong, X. Analysis of droplet stability after ejection from an inkjet nozzle. *J. Fluid Mech.* **2018**, *845*, 378–391. [CrossRef]

75. Martin, G.D.; Hoath, S.D.; Hutchings, I.M. Inkjet printing—The physics of manipulating liquid jets and drops. *J. Phys. Conf. Ser.* **2008**, *105*, 012001. [CrossRef]

76. Reis, N.; Derby, B. Ink Jet Deposition of Ceramic Suspensions: Modeling and Experiments of Droplet Formation. *MRS Proc.* **2000**, *625*. [CrossRef]

77. Derby, B. Inkjet printing ceramics: From drops to solid. *J. Eur. Ceram. Soc.* **2011**, *31*, 2543–2550. [CrossRef]

78. Jang, D.; Kim, D.; Moon, J. Influence of Fluid Physical Properties on Ink-Jet Printability. *Langmuir* **2009**, *25*, 2629–2635. [CrossRef] [PubMed]

79. Perelaer, J.J.; Smith, P.J.; Wijnen, M.M.P.; Bosch, E.V.D.; Eckardt, R.R.; Ketelaars, P.H.J.M.; Schubert, U.S. Droplet Tailoring Using Evaporative Inkjet Printing. *Macromol. Chem. Phys.* **2009**, *210*, 387–393. [CrossRef]

80. Liu, Y.-F.; Tsai, M.-H.; Pai, Y.-F.; Hwang, W.-S. Control of droplet formation by operating waveform for inks with various viscosities in piezoelectric inkjet printing. *Appl. Phys. A* **2013**, *111*, 509–516. [CrossRef]

81. Shin, P.; Sung, J.; Lee, M.H. Control of droplet formation for low viscosity fluid by double waveforms applied to a piezoelectric inkjet nozzle. *Microelectron. Reliab.* **2011**, *51*, 797–804. [CrossRef]

82. Delrot, P.; Modestino, M.A.; Gallaire, F.; Psaltis, D.; Moser, C. Inkjet Printing of Viscous Monodisperse Microdroplets by Laser-Induced Flow Focusing. *Phys. Rev. Appl.* **2016**, *6*, 024003. [CrossRef]

83. Choi, I.H.; Kim, Y.K.; Lee, S.; Lee, S.H.; Kim, J. A Pneumatic Drop-on-Demand Printing System With an Extended Printable Liquid Range. *J. Microelectromec. Syst.* **2015**, *24*, 768–770. [CrossRef]

84. Tyler, H. Open Source Possibilities for Inkjet 3D Printing, 2014. Advanced Manufacturing Research Institute, Rice University. Available online: https://www.scribd.com/document/414152953/Open-Source-Possibilities-for-Inkjet-3D-Printing-Advanced-Manufacturing-Research-Institute-Rice-University-Harrison-Tyler-2014 (accessed on 14 September 2021).

85. Fromm, J.E. Numerical Calculation of the Fluid Dynamics of Drop-on-Demand Jets. *IBM J. Res. Dev.* **1984**, *28*, 322–333. [CrossRef]

86. Nallan, H.C.; Sadie, J.A.; Kitsomboonloha, R.; Volkman, S.K.; Subramanian, V. Systematic Design of Jettable Nanoparticle-Based Inkjet Inks: Rheology, Acoustics, and Jettability. *Langmuir* **2014**, *30*, 13470–13477. [CrossRef]

87. Hoath, S.D.; Hsiao, W.-K.; Jung, S.; Martin, G.D.; Hutchings, I.M.; Morrison, N.F.; Harlen, O.G. Drop Speeds from Drop-on-Demand Ink-Jet Print Heads. *J. Imaging Sci. Technol.* **2013**, *57*, 1–11. [CrossRef]

88. Elshof, J.E.T.; Boeijsma, J. Influence of iron content on cell parameters of rhombohedral $La_{0.6}Sr_{0.4}Co_{1-y}Fe_yO_3$. *Powder Diffr.* **1996**, *11*, 240–245. [CrossRef]

89. Sammes, N. Ionic conductivity of ceria/yttria stabilized zirconia electrolyte materials. *Solid State Ionics* **1997**, *100*, 39–44. [CrossRef]

90. Lamas, D.G.; De Reca, N.E.W. X-ray diffraction study of compositionally homogeneous, nanocrystalline yttria-doped zirconia powders. *J. Mater. Sci.* **2000**, *35*, 5563–5567. [CrossRef]

91. Almar, L.; Colldeforns, B.; Yedra, L.; Estradé, S.; Peiró, F.; Morata, A.; Andreu, T.; Tarancón, A. High-temperature long-term stable ordered mesoporous Ni–CGO as an anode for solid oxide fuel cells. *J. Mater. Chem. A* **2013**, *1*, 4531–4538. [CrossRef]

92. Sanna, C.; Zhang, W.; Costamagna, P.; Holtappels, P. Synthesis and electrochemical characterization of $La_{0.6}Sr_{0.4}Co_{0.2}Fe_{0.8}O_{3-\delta}$/ $Ce_{0.9}Gd_{0.1}O_{1.95}$ co-electrospun nanofiber cathodes for intermediate-temperature solid oxide fuel cells. *Int. J. Hydrogen Energy* **2020**, *46*, 13818–13831. [CrossRef]

93. Nielsen, J.; Jacobsen, T.; Wandel, M. Impedance of porous IT-SOFC LSCF:CGO composite cathodes. *Electrochim. Acta* **2011**, *56*, 7963–7974. [CrossRef]

94. Ghatee, M.; Shariat, M.; Irvine, J. Investigation of electrical and mechanical properties of 3YSZ/8YSZ composite electrolytes. *Solid State Ionics* **2009**, *180*, 57–62. [CrossRef]

95. Nechache, A.; Cassir, M.; Ringuedé, A. Solid oxide electrolysis cell analysis by means of electrochemical impedance spectroscopy: A review. *J. Power Sources* **2014**, *258*, 164–181. [CrossRef]

96. Baiutti, F.; Blanco-Portals, J.; Anelli, S.; Torruella, P.; López-Haro, M.; Calvino, J.; Estradé, S.; Torrell, M.; Peiró, F.; Tarancón, A. Tailoring the Transport Properties of Mesoporous Doped Cerium Oxide for Energy Applications. *J. Phys. Chem. C* **2021**, *125*, 16451–16463. [CrossRef]

97. Baumann, F.S.; Fleig, J.; Habermeier, H.; Maier, J. Impedance spectroscopic study on well-defined $(La,Sr)(Co,Fe)O_{3-\delta}$ model electrodes. *Solid State Ionics* **2006**, *177*, 1071–1081. [CrossRef]

98. Carey, P.H.; Ren, F.; Hays, D.C.; Gila, B.P.; Pearton, S.J.; Jang, S.; Kuramata, A. Band alignment of atomic layer deposited SiO_2 and $HfSiO_4$ with β-Ga_2O_3. *Jpn. J. Appl. Phys.* **2017**, *56*, 071101. [CrossRef]

99. Xu, X.; Jiang, Z.; Fan, X.; Xia, C. LSM–SDC electrodes fabricated with an ion-impregnating process for SOFCs with doped ceria electrolytes. *Solid State Ionics* **2006**, *177*, 2113–2117. [CrossRef]

100. Ghom, S.A.; Zamani, C.; Nazarpour, S.; Andreu, T.; Morante, J. Oxygen sensing with mesoporous ceria–zirconia solid solutions. *Sens. Actuators B Chem.* **2009**, *140*, 216–221. [CrossRef]

101. Druce, J.; Kilner, J.A. Improvement of Oxygen Surface Exchange Kinetics for CGO with Surface Treatment. *J. Electrochem. Soc.* **2013**, *161*, F99–F104. [CrossRef]